Review of Scientific Instruments

# Development of an electron-ion coincidence apparatus for molecular-frame electron energy loss spectroscopy studies

Cite as: Rev. Sci. Instrum. **89**, 043105 (2018); https://doi.org/10.1063/1.5025773
Submitted: 13 February 2018 . Accepted: 27 March 2018 . Published Online: 18 April 2018

Noboru Watanabe, Tsukasa Hirayama, So Yamada, and Masahiko Takahashi

# Development of an electron-ion coincidence apparatus for molecular-frame electron energy loss spectroscopy studies

Noboru Watanabe,[a] Tsukasa Hirayama, So Yamada, and Masahiko Takahashi
*Institute of Multidisciplinary Research for Advanced Materials, Tohoku University, Sendai 980-8577, Japan*

(Received 13 February 2018; accepted 27 March 2018; published online 18 April 2018)

We report details of an electron-ion coincidence apparatus, which has been developed for molecular-frame electron energy loss spectroscopy studies. The apparatus is mainly composed of a pulsed electron gun, an energy-dispersive electron spectrometer, and an ion momentum imaging spectrometer. Molecular-orientation dependence of the high-energy electron scattering cross section can be examined by conducting measurements of vector correlation between the momenta of the scattered electron and fragment ion. Background due to false coincidences is significantly reduced by introducing a pulsed electron beam and pulsing scheme of ion extraction. The experimental setup has been tested by measuring the inner-shell excitation of $N_2$ at an incident electron energy of 1.5 keV and a scattering angle of 10.2°. *Published by AIP Publishing.* https://doi.org/10.1063/1.5025773

## I. INTRODUCTION

High-energy angle-resolved electron-energy-loss spectroscopy (EELS) is now a well-established technique for investigating electronic structures and electron excitation processes of atoms and molecules.[1–7] It is an electron inelastic scattering experiment in which the scattering cross section is measured as a function of energy and momentum transferred from the incident electron to the target. Within the first Born approximation, the double-differential cross section is proportional to the generalized oscillator strength (GOS), $\mathrm{d}f(\boldsymbol{K}, E)/\mathrm{d}E$,[1]

$$\frac{\partial^2\sigma}{\partial\Omega\partial E} = \frac{|\boldsymbol{k}_1|}{|\boldsymbol{k}_0|}\frac{2}{K^2E}\frac{df(\boldsymbol{K},E)}{dE}. \tag{1}$$

Here $\boldsymbol{k}_0$ and $\boldsymbol{k}_1$ are the momenta of the incident and scattered electrons, $\boldsymbol{K}$ ($=\boldsymbol{k}_0 - \boldsymbol{k}_1$) denotes the momentum transfer, and $E$ denotes the electron energy loss. GOS is defined as

$$\frac{df(\boldsymbol{K},E)}{dE} = \frac{2E}{K^2}\sum_{\mathrm{n}}\left|\langle\Phi_{\mathrm{n}}|\sum_j \exp\left(i\boldsymbol{K}\cdot\boldsymbol{r}_j\right)|\Phi_0\rangle\right|^2\delta\left(E - E_{\mathrm{n0}}\right), \tag{2}$$

where $\Phi_0$ and $\Phi_{\mathrm{n}}$ represent the wave functions of the initial and final target states, respectively, $E_{\mathrm{n0}}$ is the energy difference between these states, and $\boldsymbol{r}_j$ is the position of the $j$th electron. This quantity is, as can be seen from Eq. (2), related to the Fourier transform of overlap between the initial- and final-state wave functions, and its momentum transfer dependence provides a wealth of information about the excited electronic states of the target. Furthermore, it gives deep insights into the nature of electron excitation processes, for instance, those mediated by non-dipole interactions, being inaccessible by photo-absorption experiments.

For molecules, however, what can be observed in EELS experiments is the quantity that is averaged over the molecular orientation, owing to the random orientation of the gaseous targets. The spherical averaging of GOS leads to a significant loss of information about the target electronic structure and electron-molecule collision dynamics. If the scattering cross section is measured in the molecular-frame, ambiguities in analysis of the spherically averaged data are removed; the experiment can thus provide information about anisotropic shapes of the molecular orbitals participating in the electron impact excitation processes and also make directly visible the stereodynamics in electron-molecule collision processes.

For electron-impact ionization or transition to a short-lived highly excited state followed by immediate Auger decay, the orientation of the target molecule can be determined if the residual ion dissociates much faster than it rotates. Since the recoil direction of the fragment ion coincides with the molecular orientation at the moment of electron collision, the scattering cross section can be measured in the molecular-frame by making coincidence detection of the scattering electron and fragment ion.

On the basis of this axial-recoil approximation,[8] the first molecular-frame experiment on electron-impact ionization (e, 2e) processes was performed by Takahashi *et al.* for $H_2$,[9,10] using an energy- and angle-dispersive electron spectrometer in conjunction with an array of single-channel ion detectors. By conducting measurements of not only the scattered electron but also the ejected electron together with $H^+$ ion, the molecular-frame (e, 2e) cross sections were obtained at an incident energy of 1.2 keV. This work has paved the way toward kinematically complete studies on electron-induced dissociative ionization, and such triple-coincidence measurements, referred to as ($e$, $2e$ + M) or ($e$, $2e$ + ion) experiments, were subsequently carried out at lower incident energies, ≤200 eV, where the scattering cross section is large, by the Heidelberg group[11–14] and the Canberra group,[15–18] employing charged-particle momentum imaging techniques. Despite the efforts made by the groups, however, an ($e$, $2e$ + ion) experiment has remained technically challenging mainly because of the extremely small cross section due to its highly differential nature. It is particularly true for high incident electron energies where the first Born approximation holds.[19]

[a]Author to whom correspondence should be addressed: noboru.watanabe.e2@tohoku.ac.jp

One might think that a molecular-frame EELS experiment can easily be performed because the slow ejected electron may be left undetected, by contrast to ($e$, $2e$ + ion) experiments, where triple-coincidence detection of three charged particles is required. However, this kind of experiment is still challenging, in particular when the magnitude of momentum transfer is sizable. In the measurements, electrons with a specific kinetic energy are selectively detected at a particular scattering angle in coincidence with fragment ions originated in collisions with the electrons detected. Nevertheless, such ions are not separable from those generated via other collisions, which lead to false coincidences, corresponding to detection of electrons and ions produced via different scattering events. Thereby, a number of ions produced through intense forward scattering cause a huge background due to false coincidences, making it difficult to extract true coincidence signals from the experimental data measured. This difficulty is a practical reason why molecular-frame studies using axial-recoil fragmentation have rarely been performed for electron-induced processes, whilst a number of such studies have been reported for photoionization of molecules.[20,21]

Under the circumstances, we have recently developed an electron-ion coincidence apparatus to realize molecular-frame EELS experiments and applied it to investigate the inner-valence ionization of $N_2$.[22,23] The vector correlation between the transferred momentum and recoil momentum of the fragment ion has been measured for the transition to the $2\sigma_g \rightarrow 1\pi_g$ autoionization state and $F\,^2\Sigma_g^+$ direct ionization at an incident electron energy of 1.4 keV. The scattering cross sections thus obtained exhibit anisotropic molecular-orientation dependence, and it has been revealed that the angular distribution appreciably changes with transferred momentum, reflecting influences of non-dipole interaction on the ionization dynamics. The studies have demonstrated that the method provides a powerful means to explore momentum-transfer-dependent stereodynamics in electron impact ionization of molecules.

In this paper, we describe details of the electron-ion coincidence apparatus and measurement scheme established for molecular-frame EELS studies at high incident electron energies. An energy-dispersive electron spectrometer and ion momentum-imaging spectrometer have been used to achieve high collection efficiency of the charged particles. Furthermore, contributions from false coincidences have significantly been reduced by introducing a high-frequency pulsed electron beam in conjunction with the pulsing scheme for ion extraction. To illustrate the performance of the apparatus, experimental results on the inner-shell excitation of $N_2$ are presented.

## II. APPARATUS

### A. Electron-ion coincidence apparatus

An electron-ion coincidence spectrometer has been developed in our laboratory. Figure 1 shows a simplified schematic of our experimental setup. The main parts of the apparatus are a pulsed electron gun, an energy-dispersive electron spectrometer, and an ion momentum imaging spectrometer. These components are housed in a cylindrical vacuum chamber

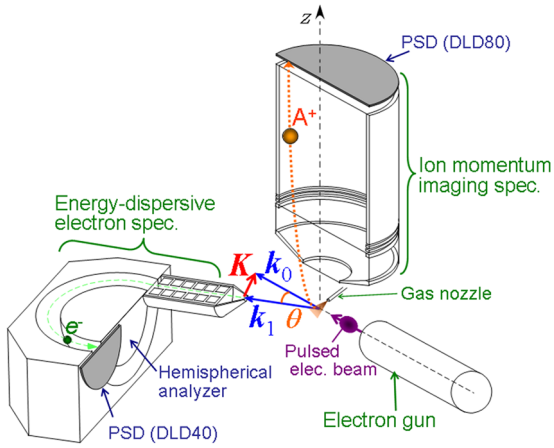


FIG. 1. A schematic representation of the experimental setup for electron-ion coincidence measurements.

with 760 mm inner diameter (i.d.), which is pumped by a 3400 $dm^3\ s^{-1}$ turbomolecular pump (OSAKA VACUUM, TG3410). The base pressure of the chamber is $\sim 1 \times 10^{-5}$ Pa. A double-layer μ-metal shield is used to reduce the ambient magnetic field to less than 2 mG.

Here we give a brief description of a measurement scheme. Details of the electron- and ion-spectrometers are described in Subsections II B–II D. A finely focused electron beam is generated by a high-current electron gun, which is similar to that developed by Erdman and Zipf,[24] combined with an electrostatic acceleration lens. The electron beam is pulsed by applying rectangular voltage pulses to a deflector electrode placed prior to the exit apertures of the electron gun. The incident electron beam is crossed with a molecular beam effusing from a gas nozzle with 0.5 mm i.d. The diameter of the electron beam at the scattering point is estimated to be ~1 mm.

Electrons scattered at a particular angle of $\theta$ with respect to the incident electron beam direction are collected by the electron spectrometer, which is mounted on a turntable. Rotation of the table is accomplished by turning a worm gear with a 720:1 and $\theta$ can be changed from −5° to 40°, the angle, which is related to the magnitude of the momentum transfer as $|\boldsymbol{K}| = \{k_0^2 + k_1^2 - 2k_0k_1\cos\theta\}^{1/2}$.

Upon detection of a scattered electron, an ion-extraction field of 33 V/cm is applied to the interaction region to push ions into the momentum imaging spectrometer. Electrodes used for ion extraction are grounded during the transmission of the electron pulse and hence, fragment ions can be collected without affecting trajectories of the electrons. The ion spectrometer is mounted in the vertical direction with respect to the scattering plane, which is defined by the momenta of the incident and scattered electrons.

The use of the above pulsing scheme allows us to measure an electron and ions produced by a single incident-electron pulse, resulting in significant reduction of background compared to cases employing a continuum electron beam.[9,10,19] However, the data obtained in this manner still involve events in which an electron and ion produced by different collisions are detected in coincidence. To estimate the background due to

the false coincidences, we also record ions generated by incident electron pulses that pass through the interaction region shortly after electron detection. The ions collected in this way are uncorrelated to the detected electron and hence provide contributions of false coincidences. The background contributions thus estimated are subtracted from the coincidence data.

### B. Energy-dispersive electron spectrometer

Figure 2 shows a cross section view of the energy-dispersive electron spectrometer, whose electrodes are fabricated from non-magnetic materials such as A7075 aluminium alloy. The spectrometer consists of entrance apertures, a seven-element electrostatic deceleration lens,[25] a hemispherical analyzer with 66.5 mm mean radius, a Herzog's plate to compensate fringing effects,[26] and a position sensitive detector (PSD), which is comprised of a pair of micro-channel plates (MCPs) with 47 mm active diameter followed by a fast position-sensitive delay-line readout (RoentDek, DLD40).[27] The inner and outer radii of the hemispherical analyzer are 48 and 85 mm, respectively. To minimize emission of secondary electrons, the surfaces of the inner- and outer-spheres as well as those of electrodes exposed to electrons are coated with colloidal graphite. To make a correction of non-uniformity of the electric field at around the fringe of the hemispherical analyzer, co-axial ring electrodes, $H_1$ and $H_2$, being similar to those introduced by Brunt *et al.*,[28] are mounted surrounding the edge of the inner half sphere.

Electrons passed through the entrance apertures are decelerated by an electrostatic lens to achieve higher energy resolution and then dispersed by the hemispherical analyzer, which is typically operated at a mean pass-energy of 53 eV. The voltages applied to $H_1$ and $H_2$ are adjusted so that the energy resolution is most improved. The energies of the electrons can be determined from their arrival positions at the PSD.

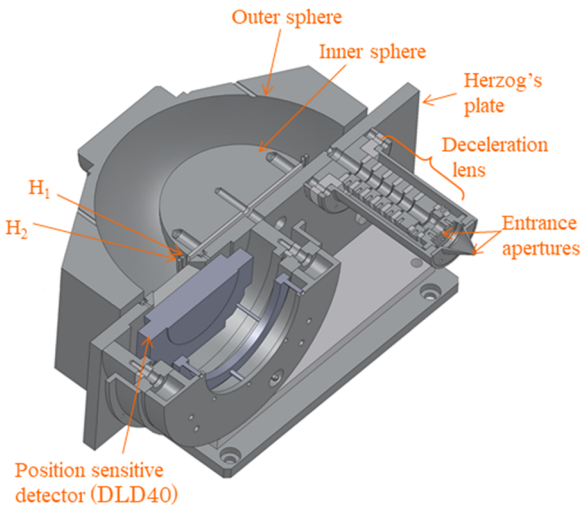


FIG. 2. A cross section view of the energy-dispersive electron spectrometer. The inner and outer radii of the hemispherical analyzer are 48 and 85 mm, respectively.

### C. Ion momentum imaging spectrometer

A schematic representation of the ion momentum imaging spectrometer is shown in Fig. 3. The spectrometer, which is similar to that developed by Lower *et al.*,[18] consists of three electrodes ($M_1$, $M_2$, and $M_3$) for creating a homogeneous electric field, a 93 mm drift tube with 90 mm i.d. equipped with a velocity mapping lens,[29,30] and a PSD. The electrodes of the spectrometer are made of A2017 aluminium. The velocity mapping lens is constructed from a pair of ring electrodes with 2 mm thickness, $L_1$ and $L_2$. The lens electrodes and a flight tube, FT, are separated from one another by a 1 mm distance. The PSD is comprised of a pair of MCPs with an active diameter of 83 mm followed by a delay-line readout (RoentDek, DLD 80).[27] The spectrometer is mounted so that its entrance is 7 mm above the interaction region and the front surface of the PSD (detection plane) is parallel to the scattering plane.

Ions produced by electron impact are extracted by applying a pulse voltage to an electrode $E_1$ placed below the interaction region while keeping the voltage of $M_1$ to be 0 V. The extraction field is typically maintained for 2.2 $\mu$s in coincidence measurements. It allows us to collect, for instance, $N^+$ ions with up to 8 eV kinetic energy over a 4π solid angle emission. The ions pushed into the spectrometer are accelerated by a dc uniform electric field generated by the $M_1$, $M_2$, and $M_3$ electrodes, equipped with an electroformed mesh with 88% transparency (Goodfellow, CU008720), and then travel through a drift region before reaching the detector. An electroformed mesh is mounted at the end of the flight tube for preventing the penetration of an electric field due to a high voltage applied to the MCP (−2180 V) into the drift region. The lengths of the extraction and drift regions, $l_e$ and $l_d$, satisfy the Wiley-McLaren condition, $l_d = 2 \times l_e$.[31]

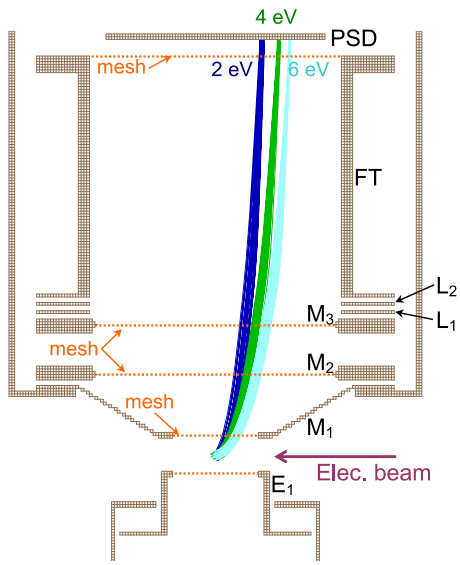


FIG. 3. A cross section view of the ion momentum imaging spectrometer as well as ion trajectories simulated for $N^+$ having kinetic energies of 2, 4, and 6 eV. A homogeneous electric field for ion extraction is created using the $E_1$, $M_1$, $M_2$, and $M_3$ electrodes, and a nonuniform electric field is generated by means of a velocity mapping lens consisting of a pair of ring electrodes, $L_1$ and $L_2$. FT denotes a flight tube, whose inner diameter is 90 mm.

Owing to the flight time of the scattered electron and the finite response time of pulse-processing electronics, the ion extraction field is turned on ~300 ns after the electron collision. This time delay results in expansion of effective interaction volume seen from the ion spectrometer because fragment ions move from the scattering point during the time. To minimize the deterioration of the momentum resolution due to the effective interaction volume, a nonuniform electric field created by the lens electrodes is optimized by means of ion-trajectory simulations so that the ions accelerated from different positions are focused onto the PSD. The simulations were carried out using 3D ion trajectory simulation software, SIMION 8.0.[32] Examples of the ion trajectories are shown in Fig. 3. In the simulation, $N^+$ ions with kinetic energies of 2, 4, and 6 eV are ejected from a spherical region with 2 mm radius and their initial emission directions are set to be parallel to the electron scattering plane. The extraction field is created by means of the $E_1$, $M_1$, $M_2$, and $M_3$ electrodes with voltages of +46, 0, −73, and −145 V, respectively, and the nonuniform field is generated by applying voltages of +950, +175, and −74 V to $L_1$, $L_2$, and FT. It can be seen from the figure that the ions having the same kinetic energy are well focussed on the PSD; the distance from the center of the detector to the arrival position is determined by the ion energy and the ratio of charge to mass.

The recoil-momentum of a detected ion is determined from its time of flight (TOF) and arrival positions at the PSD. If the nonuniform electric field is not applied to the drift region, the $x$-, $y$-, and $z$-direction components of the recoil-momentum, $p_x$, $p_y$, and $p_z$, can simply be expressed as

$$p_x = mx/T, \quad p_y = my/T, \quad p_z = q(T - T_0)E_{\text{ext}},$$

where $m$ and $q$ are the mass and charge of the ion, $T$ denotes its TOF, and $E_{\text{ext}}$ is the magnitude of the extraction field. Here the z-axis is taken to be perpendicular to the detection plane and the ion arrival position at the PSD is given by $(x, y)$. $T_0$ represents TOF for an ion whose initial kinetic energy is zero, and its arrival position is set to $x = y = 0$. The above relationships are, however, modified by the introduction of the nonuniform electric field. We have thus examined the actual relation of the initial momentum to a set of parameters $(x, y, T)$ for each ion species by means of ion-trajectory simulations, and the results have been used in the analysis of experimental data.

### D. Data acquisition system

For coincidence measurements, there exists a trade-off between the incident beam intensity and the ratio of the false coincidence signals involved. A larger number of electrons in a single electron pulse cause a higher count rate but result in a lower signal-to-background ratio. It is therefore desirable to use a pulsed electron beam with a smaller number of electrons in each pulse but with higher frequency to compensate for the reduction of the incident beam current. We have thus developed the following measurement scheme using a high-frequency pulsed electron beam.

A schematic of the data acquisition system and the timing diagram for coincidence measurements are shown in Fig. 4. An incident electron pulse is emerged by applying a rectangular voltage pulse supplied from a function generator

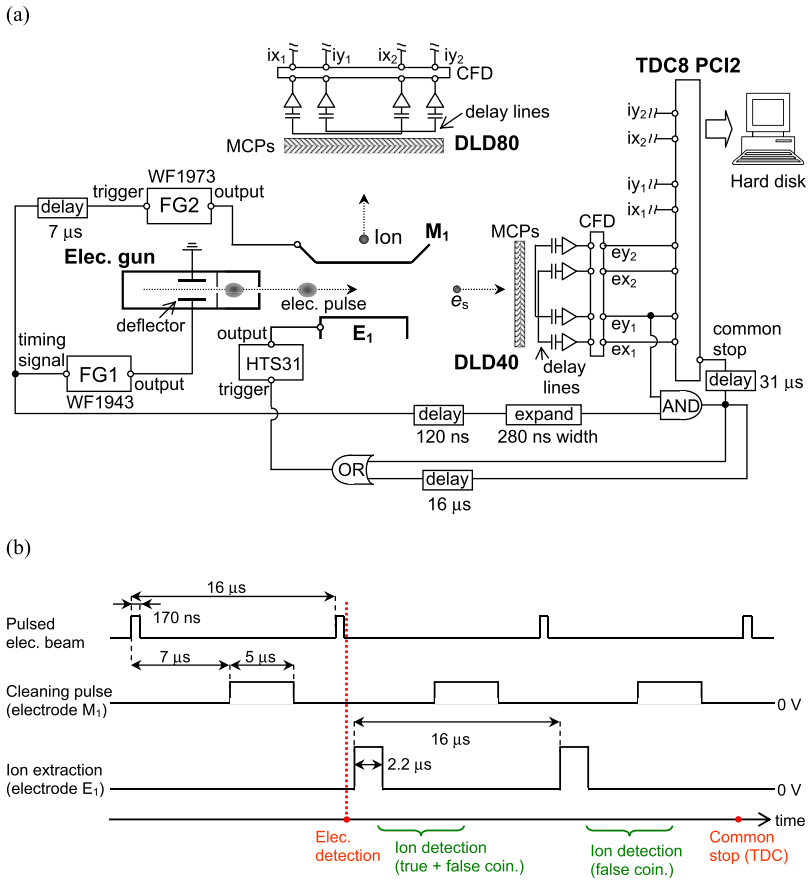


FIG. 4. (a) Data acquisition system and (b) timing diagram for electron-ion coincidence measurements.

(NF Electronic Instruments, Wave Factory WF1943), FG1, to a deflector electrode of the electron gun. The temporal width and repetition frequency of the pulse electron beam are typically 170 ns and 62.5 kHz, respectively. The separation in time between successive electron pulses is thus 16 $\mu$s. The function generator also outputs a synchronized timing signal, which is divided into two signals. The first one is delayed by 7 $\mu$s and used to control another function generator (NF Electronic Instruments, Wave Factory WF1973), FG2. A positive voltage pulse generated by FG2 is applied to the electrode $M_1$, which is located at the entrance of the ion spectrometer, for cleaning up the interaction region by removing slow parent ions produced by electron collision. The second signal is made to have a 280 ns width after being delayed by 120 ns for further processing.

For arrival of an electron, the DLD40 detector produces four separate output signals ($ex_1$, $ex_2$, $ey_1$, $ey_2$) from the ends of two orthogonal delay lines. Here $ex_1$ and $ex_2$ are signals from the delay line associated with the energy-dispersive direction and $ey_1$ and $ey_2$ are those from the other delay line. These four signals are accepted by a module which involves a 6-fold differential amplifier with an integrated constant fraction discriminator (CFD) circuit for each channel (RoentDek, DLATR6). The amplified signals are discriminated from noise and converted to logic signals by the DLATR6 module. One of the converted signals, $ey_1$, is then divided into two signals. The first one and the other three delay-line signals are fed to the first four of eight independent input channels of a time-to-digital converter (TDC), which is operated in the "common-stop" mode. The TDC used (RoentDek, TDC8 PCI2[27]) has a time resolution of 0.5 ns. An AND logic operation is then applied to the remaining second signal and the 280 ns width signal mentioned above. The AND gate output is a sign that an electron originated from the incident electron pulse is detected.

Subsequently, the output signal from the AND gate is divided into three signals. The first one triggers an ion extraction field, which is created by applying a positive voltage pulse to the $E_1$ electrode using a transistor switch (Behlke, HTS31) combined with a DC power supply. The second signal is delayed by 16 $\mu$s and then used as a trigger of an additional ion-extraction field, which is generated for collecting ions produced by an incident electron pulse emitted just after the electron detection. As mentioned above, the ions recorded in this manner provide contributions from false coincidences. For each arrival of an ion, the DLD80 detector produces four delay-line signals ($ix_1$, $ix_2$, $iy_1$, $iy_2$), which are converted to logic signals using an amplifier and a CFD module (RoentDek, ATR19) and then fed to the latter four input channels of the TDC. For each event, the input channels of the TDC can accept up to 16 signals and hence multiple ions in a given extraction can be measured. The remaining third signal is delayed by 31 $\mu$s and then used as a timing signal (common stop signal) for the TDC. The data collected by the input channels during a 32 $\mu$s period before the acceptance of the timing signal are recorded on a hard disk (HD) using a data gathering program (RoentDek, CoboldPC).

The arrival position and arrival time of an ion at the DLD80 detector can be encoded from the data stored in the HD. We now consider the times of arrival at the TDC for signals from the ends of two delay lines of DLD80 and denote those as $t_{ix1}$, $t_{ix2}$, $t_{iy1}$, and $t_{iy2}$, respectively. Here $t_{ix1}(t_{iy1})$ represents the time for a signal from one end of the delay line associated with the $x$-direction ($y$-direction) and $t_{ix2}(t_{iy2})$ is that for its counterpart signal from the other end. Since an electric pulse propagates on a delay line at a constant speed, the following relations hold:

$$(t_{ix1} - t_i) + (t_{ix2} - t_i) = C_x,$$
$$(t_{iy1} - t_i) + (t_{iy2} - t_i) = C_y,$$

where $C_x$ and $C_y$ are constant values for the delay lines and $t_i$ denotes the arrival time of the ion at the detector. By using the relations, $t_i$ can be obtained. Besides, the difference in time between pulses from both ends of each delay line allows us to determine the arrival position of the ion ($x_i$, $y_i$) as follows:

$$x_i = v_x(t_{ix1} - t_{ix2}),$$
$$y_i = v_y(t_{iy1} - t_{iy2}).$$

Here $v_j$ ($j = x$ or $y$) is the effective perpendicular propagation speed on the delay line. Similarly, the arrival position and arrival time of an electron at the DLD40 detector can be encoded from the data recorded for each event.

## III. CHARACTERIZATION OF ELECTRON AND ION DETECTION

### A. Energy calibration of the electron spectrometer

Energy calibration of the electron spectrometer has been made by measuring elastically scattered electrons, whose energies are the same as the incident electron energy. Here we illustrate an example of the energy calibration procedure, performed in our previous work for studying inner-valence ionization of $N_2$.[23] In the procedure, a series of measurements on elastic scattering were carried out with varying incident electron energy from 1364 to 1373 eV with 1 eV step. Scattered electrons were decelerated to ~53 eV using the electrostatic lens system prior to energy analysis. The deceleration rate and the mean-pass energy of the hemispherical analyzer were kept constant during the measurements.

Figure 5(a) shows the peak profiles of elastic scattering measured at different incident electron energies. A Gaussian function was fitted to each spectrum for obtaining the peak position and width. The data presented in Fig. 5(b) are the relation between the electron energy and arrival position at the detector thus obtained. A quadratic polynomial was employed as a fitting function. It can be seen from the figure that the experimental result is satisfactorily reproduced by the fitted function. The instrumental energy resolution was determined from the widths of the peak profiles to be 0.8–0.9 eV FWHM (full width at half maximum) over the energy region covered.

### B. Momentum resolution of the ion spectrometer

The momentum resolution of the ion spectrometer has been estimated by recording fragment ions generated through

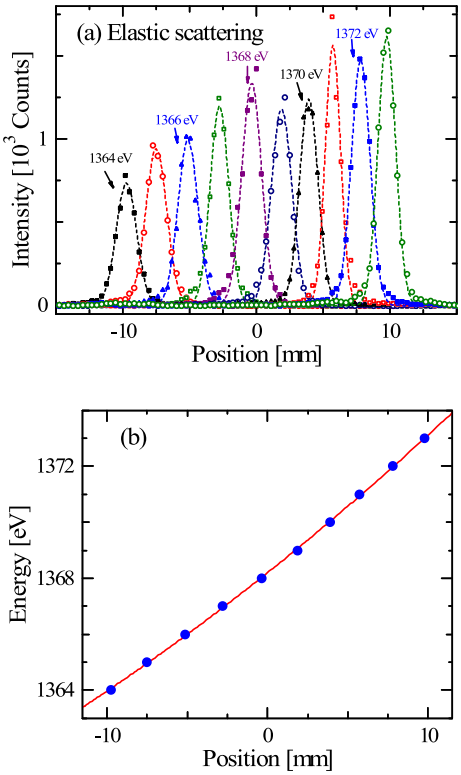


FIG. 5. (a) Peak profiles of elastic scattering measured at incident electron energy from 1364 to 1373 eV with 1 eV step. Dashed lines are Gaussian functions fitted to the individual spectra. (b) The relation between the electron energy and arrival position at the position sensitive detector (DLD40). The solid line is a fitting function.

the dissociative double-ionization of CO. Owing to momentum conservation, the sum of recoil momenta of two fragments produced via $CO^{2+} \rightarrow C^+ + O^+$ should be zero: $\boldsymbol{p}_1 + \boldsymbol{p}_2 = 0$, where $\boldsymbol{p}_1$ and $\boldsymbol{p}_2$ are the momenta of $C^+$ and $O^+$, respectively. Thereby, the width of the experimental $\boldsymbol{p}_1 + \boldsymbol{p}_2$ distribution reflects the momentum resolution of the measurement system, which depends on the position- and time-resolutions of the detector used, size of the interaction region, and thermal distribution of the target molecules.

Ions produced by electron impact on CO were measured at an incident electron energy of 1.4 keV. Figure 6 shows the time correlation map of ion pairs detected in coincidence. Here TOF1 represents the time of flight of the first-hit ion and TOF2 is that of the second-hit ion. Inserted in the figure is the ion TOF spectrum of CO; $C^+$ and $O^+$ are observed as broad bands centred at around 4.2 and 4.9 $\mu$s, respectively. In the correlation map, a diagonal island appears in the region of TOF1 ~ 3.6–4.6 $\mu$s and TOF2 ~ 4.5–5.3 $\mu$s, which can be attributed to the $C^+ + O^+$ dissociation.

From the coincidence data, the $\boldsymbol{p}_1 + \boldsymbol{p}_2$ distribution was constructed. Its x-, y-, and z-direction components are presented in Fig. 7. Here the TOF axis of the ion spectrometer is taken as the z-axis. From FWHMs of the peak profiles, the momentum resolution has been determined to be $\Delta p_x \sim 20.0$ a.u., $\Delta p_y \sim 18.3$ a.u., and $\Delta p_z \sim 12.3$ a.u. The results are comparable to those of ion momentum imaging spectrometers developed by Wang *et al.* ($\Delta p_x \sim 24.8$ a.u., $\Delta p_y \sim 15.9$ a.u., and $\Delta p_z \sim 17.8$ a.u.)[33] and Singh *et al.*

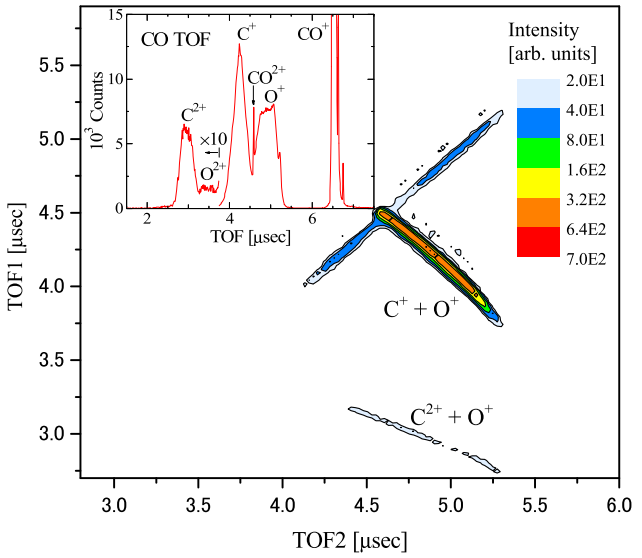


FIG. 6. Time correlation map of ion-pairs detected in coincidence for CO. TOF1 (TOF2) represents the time of flight of the first-hit ion (second-hit ion). Inserted in the figure is the ion TOF spectrum of CO.

($\Delta p_y \sim 15$ a.u., and $\Delta p_z \sim 10$ a.u.)[34] for investigating dynamics of electron-induced molecular fragmentation.

We subsequently obtained a kinetic energy release (KER) distribution for the $C^+$ and $O^+$ ion pairs. Figure 8 shows a comparison of the result with the corresponding distribution reported by Pandey *et al.*,[35] which was measured at an incident electron energy of 1 keV. It can be seen from the figure that the results of the two experiments are in good accordance with each other.

## IV. SAMPLE RESULTS

To test the performance of the apparatus, an electron-ion coincidence experiment was carried out for the inner-shell excitation of $N_2$ at $E_0 = 1.5$ keV with a scattering angle of $\theta = 10.2°$, which corresponds to $K^2 = 5.3$ a.u. In the measurement, commercially available $N_2$ gas (>99.999 95%, Taiyo Nippon Sanso Co.) was used without further purification. The experimental result was obtained by accumulating data at an ambient sample gas pressure of $1.0 \times 10^{-4}$ Pa for 5 weeks' runtime.

In Fig. 9, we present the ion TOF spectrum of $N_2$, constructed from the electron-ion coincidence data. Also depicted in the figure is the background due to false coincidences, which was inferred from events of detecting an electron and ion produced by two-different incident electron pulses, as mentioned in Sec. II. It can be seen from the figure that the spectrum exhibits about a factor of 2 higher intensity than the background at TOF = 4–5 $\mu$s, where $N^+$ fragment ions are detected. It is an unambiguous proof of the capability of the present method to observe the electron-$N^+$ true-coincidence signals even for the inner-shell excitation, despite its small scattering cross section[3] and despite a number of non-correlated ions being formed through intense valence ionization.

Figure 10 presents a fragment-ion yield spectrum, which was constructed by plotting the number of the electron-$N^+$

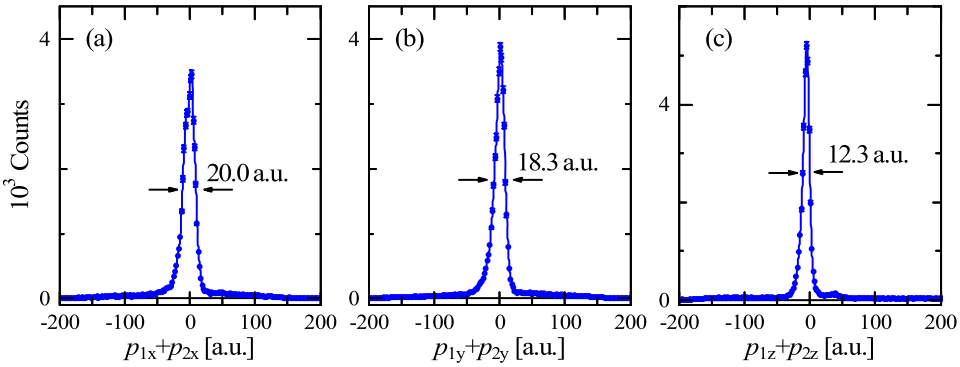


FIG. 7. Distributions of three components of $\boldsymbol{p}_1 + \boldsymbol{p}_2$, constructed from the $C^+$ and $O^+$ coincidence data. (a) The x-direction, (b) the y-direction, and (c) the z-direction components.

true-coincidence evens as a function of electron energy loss. Vertical bars indicate excitation energies of $N_2$ reported in the literature.[36] A strong peak is observed at 401 eV, which can be ascribed to excitation of an electron from the $1\sigma_g$ or $1\sigma_u$ core orbital to the $1\pi_g$ lowest unoccupied orbital. It has often been referred to as "$\pi^*$ resonance." The $(1\sigma_g)^{-1}(1\pi_g)^1$ and $(1\sigma_u)^{-1}(1\pi_g)^1$ $N_2$ excited states formed via the $\pi^*$ resonance may decay into an ion state through Auger emission and then dissociate.[36] The $\pi^*$ resonance has been observed also in the photoabsorption spectrum, but it is attributed only to $1\sigma_u \rightarrow 1\pi_g$ since the other is optically forbidden. In contrast to photoabsorption, not only $1\sigma_u \rightarrow 1\pi_g$ but also $1\sigma_g \rightarrow 1\pi_g$ can be induced by electron impact,[4,37] whilst they are indistinguishable from each other in the measurement due to their small energy separation, which has theoretically been predicted to be 220 meV by Butscher *et al.*[38] and 60 meV by Rescigno and Orel.[39] The right panel of Fig. 10 presents the kinetic energy distribution of $N^+$ generated via the $\pi^*$ resonance. It exhibits a broad distribution with a maximum at KE ~ 4 eV as well as an intense thermal energy component around 0 eV.[40]

We subsequently examine the molecular-orientation dependence of the $\pi^*$ resonance. Figure 11 presents the molecular-frame electron scattering cross section for the 401 eV band, $\sigma(\boldsymbol{K})$, which was obtained by plotting the number of the true coincidence events with $N^+$ having KE = 3.0-6.5 eV as a function of the angle made between the momentum transfer vector $\boldsymbol{K}$ and the molecular-axis, $\phi_{\boldsymbol{K}}$. The thermal energy component, with low KE of $N^+$, was not included in the analysis because the axial-recoil approximation may possibly be invalid for the associated dissociation process. A glance of Fig. 11 shows that $\sigma(\boldsymbol{K})$ exhibits distinct molecular orientation dependence and that the $\pi^*$ resonance preferentially occurs when the molecular axis is perpendicular to $\boldsymbol{K}$.

To get further insights into the molecular-orientation dependence, an *ab initio* calculation was conducted at the level of time-dependent density functional theory (TDDFT) with the PBE0 functional[41] using the correlation-consistent polarization core-valence-triple-zeta basis set augmented with diffuse functions, aug-cc-pCVTZ.[42,43] In the calculation, the General Atomic Molecular Electronic Structure System (GAMESS) program[44] was used. The $(1\sigma_g)^{-1}(1\pi_g)^1$ and $(1\sigma_u)^{-1}(1\pi_g)^1$ core excited states have been found at excitation energies of 389.66 and 389.68 eV, which considerably underestimate the experimental value. The disagreement may be due mainly to self-interaction effects.[45] By using the transition density matrix obtained from the TDDFT calculation, GOSs were computed for the $1\sigma_u \rightarrow 1\pi_g$ and $1\sigma_g \rightarrow 1\pi_g$ excitations. Also calculated was the optical oscillator strength of the $\pi^*$ resonance, $f$. The obtained value, $f = 0.22$, is in fair agreement with the experimental results reported in the literature, $f = 0.18$–$0.23$.[4] The theoretical GOSs of the individual transitions are shown in Fig. 11 as dashed and dashed-dotted lines, together with their sum as a solid line. For comparison in shape, the associated theoretical curve was scaled to the experiment at $\phi_{\boldsymbol{K}} = 85°$. It can be seen from the figure that the TDDFT calculation well accounts for the experimental result.

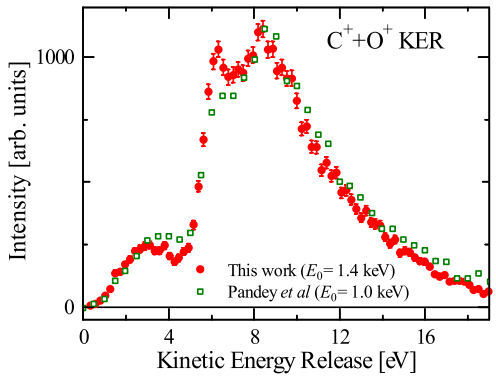


FIG. 8. Kinetic energy release distribution for the $C^+$ and $O^+$ ion pair. Open squares represent the corresponding result of an experiment by Pandey *et al.* at $E_0 = 1$ keV.[35]

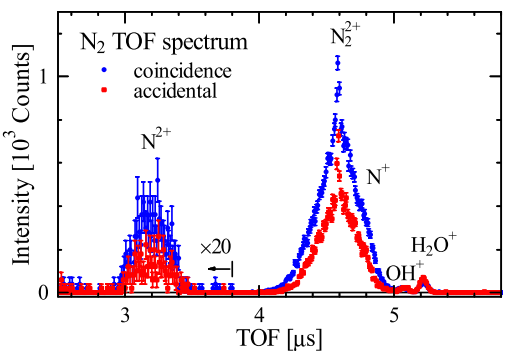


FIG. 9. Ion TOF spectrum of $N_2$. The solid circles represent the electron-$N^+$ coincidence data, while the squares correspond to the background due to false coincidences (see the text for details).

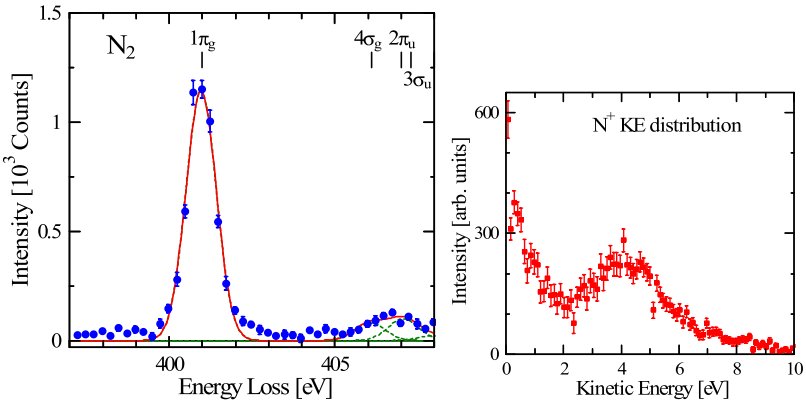


FIG. 10. Fragment-ion yield spectrum of $N_2$ at $K^2 = 5.3$ a.u., constructed by plotting the number of electron-$N^+$ true coincidence events as a function of electron energy loss (left panel) and the kinetic energy distribution of $N^+$ for the $\pi^*$ resonance (right panel).

Also seen from the figure is that there is a significant difference between the theoretical results of the two inner-shell excitations. For instance, at $\phi_{\boldsymbol{K}} \sim 90°$, the excitation from the $1\sigma_u$ orbital exhibits a maximum, while that from the $1\sigma_g$ orbital has zero intensity. It indicates that $\sigma(\boldsymbol{K})$ exhibits an angular distribution being characteristic for each electron excitation, depending upon the spatial shapes of molecular orbitals participating in the excitation process.

The difference between the angular distributions can qualitatively be understood using a simple model. Within the linear combination of atomic orbital (LCAO) approximation, the inner-shell orbitals are written as $\psi_{i\pm}(\boldsymbol{r}) = C_{i\pm}\{\chi_{1s}(\boldsymbol{r} - \boldsymbol{R}_1) \pm \chi_{1s}(\boldsymbol{r} - \boldsymbol{R}_2)\}$, where $\chi_{1s}(\boldsymbol{r} - \boldsymbol{R}_j)$'s (j = 1 or 2) denote the constituent 1s atomic orbital (AO) centred at the j-th N atom and $C_{i\pm}$ is the normalization factor. The plus sign corresponds to the $1\sigma_g$ orbital and the minus sign corresponds to the $1\sigma_u$ orbital. Similarly the $1\pi_g$ orbital is expressed as $\psi_f(\boldsymbol{r}) = C_f\{\chi_{2p}(\boldsymbol{r} - \boldsymbol{R}_1) - \chi_{2p}(\boldsymbol{r} - \boldsymbol{R}_2)\}$ with $\chi_{2p}$ being the N 2p AO directed perpendicular to the molecular axis, where $C_f$ is the normalization factor. Since each 1s orbital is highly localized on an N atom, overlaps between the AOs centered at different atoms are quite small. It follows from this fact and a single electron approximation that the GOSs of the inner-shell excitations can be approximated as

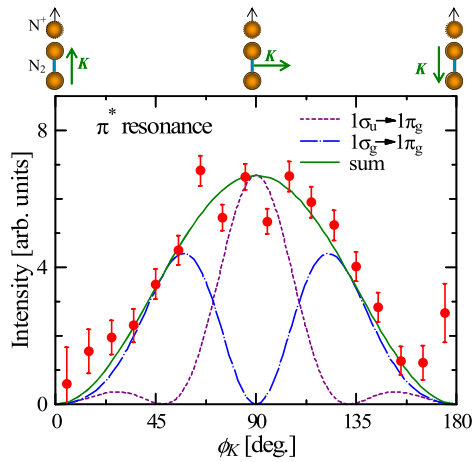


FIG. 11. Molecular-frame electron scattering cross section for the $\pi^*$ resonance of $N_2$. For comparison, TDDFT calculations for the $1\sigma_u \rightarrow 1\pi_g$ and $1\sigma_g \rightarrow 1\pi_g$ excitations are presented as dashed- and dashed-dotted lines, respectively, together with their sum as a solid line.

$$
\begin{aligned}
f(\boldsymbol{K}) &\approx \frac{2E}{K^2}\left|\left\langle\psi_f\right|\exp(i\boldsymbol{K}\cdot\boldsymbol{r})\left|\psi_{i\pm}\right\rangle\right|^2 \\
&\approx \frac{2E}{K^2}\left|C_{i\pm}C_f\left\langle\chi_{2p}\right|e^{i\boldsymbol{K}\cdot\boldsymbol{r}}\left|\chi_{1s}\right\rangle\{\exp(i\boldsymbol{K}\cdot\boldsymbol{R}_1)\right. \\
&\quad \left.\mp\exp(i\boldsymbol{K}\cdot\boldsymbol{R}_2)\}\right|^2 \\
&= \frac{4E}{K^2}{C_{i\pm}}^2{C_f}^2\left|\left\langle\chi_{2p}\right|e^{i\boldsymbol{K}\cdot\boldsymbol{r}}\left|\chi_{1s}\right\rangle\right|^2\{1\mp\cos[\boldsymbol{K}\cdot(\boldsymbol{R}_2-\boldsymbol{R}_1)]\}.
\end{aligned}
$$

Here $\{1 \mp \cos[\boldsymbol{K}\cdot(\boldsymbol{R}_1 - \boldsymbol{R}_2)]\}$ represents an interference factor arising from coherent excitation from the two equivalent 1s AOs, and it is the source of the observed difference between the theoretical angular distributions. It implies that the measurement of the individual molecular-frame scattering cross sections for these inner-shell excitations can be regarded as a molecular double-slit experiment. A similar Young-type interference has been observed by photon- and charged-particle-impact ionization studies for molecules,[46] and it has been shown that the interference pattern may provide a wealth of information about not only the molecular geometry but also the spatial distribution and symmetry of the associated molecular orbitals.[47,48] Unfortunately, however, the sum of the GOSs smears out the interference and as a consequence, the observed angular distribution is simply proportional to $(2E/K^2)|\langle\chi_{2p}|\exp(i\boldsymbol{K}\cdot\boldsymbol{r})|\chi_{1s}\rangle|^2$, which corresponds to the GOS of the 1s → 2p excitation in a nitrogen atom. Here it may be of interest to note that although the interference effect has not experimentally been identified for the inner-shell single-electron excitation, our previous study on the inner-valence region has revealed that the scattering cross section of the $2\sigma_g \rightarrow 1\pi_g$ dipole-forbidden transition exhibits an angular distribution being similar to the theoretical prediction for the $1\sigma_g \rightarrow 1\pi_g$ inner-shell excitation,[22] and its minimum observed at $\phi_{\boldsymbol{K}} \sim 90°$ can be accounted for as a result of the interference effect. It strongly suggests that the present technique offers an opportunity to examine the interference effects for fixed-in-space molecules, which can be used to infer the symmetry and phase of associated molecular orbitals.

## V. SUMMARY

In this article, we have described the development of an experimental setup for molecular-frame EELS studies at high incident electron energies. The coincidence detection of

electrons and ions enables us to determine the electron scattering cross section for targets with the direction of the molecular-axis being specified. By introducing a pulsing scheme for ion extraction, background due to uncorrelated-ions has significantly been reduced.

To assess the performance of the apparatus, an electron-ion coincidence experiment was carried out for the inner-shell excitation of $N_2$. It has demonstrated the capability of the present method to observe electron-ion coincidence signals for inner-shell excitation, despite the scattering cross section being several orders of magnitude smaller than that of valence ionization.[3] The angular distribution thus obtained exhibits clear molecular orientation dependence, and it has been shown that the $\pi^*$ resonance preferentially occurs for molecules with the axis perpendicular to $\boldsymbol{K}$ under the experimental conditions used.

The electron-ion coincidence technique can provide a powerful means for investigating not only dipole-allowed transitions but also dipole-forbidden transitions, being inaccessible by photoabsorption experiments, and their decay dynamics in detail. The determination of the vector correlation between the momenta of the scattered electron and the fragment ion would be of great assistance to elucidate the dynamics of electron-induced dissociative-ionization, which has been inferred from the partial ionization cross sections and kinetic energy distributions of fragments so far.[49–51] It enables one to examine how the reaction probability to produce a particular fragment depends upon the energy- and momentum-transferred from the projectile electron to the target.[23] Furthermore, the technique makes it possible to explore the stereodynamics in electron induced excitations, which depend upon the anisotropic shape of associated molecular orbitals. We expect that future efforts will be dedicated along these lines to various molecular targets to enrich molecular-frame EELS studies. For the purpose, it would be desirable to use an energy- and angle-dispersive electron spectrometer[52] that significantly improves the instrumental sensitivity.

## ACKNOWLEDGMENTS

The authors thank the technical staff of the machine shop at the Institute of Multidisciplinary Research for Advanced Materials for their expertise and skills in developments of the apparatus. This research was supported by the JSPS KAKENHI Grant Nos. JP15H03761, JP25620006, and JP25248002.

[1] M. Inokuti, Rev. Mod. Phys. **43**, 297 (1971).
[2] K. T. Leung, J. Electron Spectrosc. Relat. Phenom. **100**, 237 (1999), and references therein.
[3] A. P. Hitchcock, J. Electron Spectrosc. Relat. Phenom. **112**, 9 (2000), and references therein.
[4] R. S. Barbieri and R. A. Bonham, Phys. Rev. A **45**, 7929 (1992).
[5] Y.-Y. Wang, J.-M. Sun, and L.-F. Zhu, J. Chem. Phys. **132**, 124301 (2010).
[6] N. Watanabe, D. Suzuki, and M. Takahashi, J. Chem. Phys. **134**, 064307 (2011).
[7] N. Watanabe, T. Hirayama, D. Suzuki, and M. Takahashi, J. Chem. Phys. **138**, 184311 (2013).
[8] R. N. Zare, Mol. Photochem. **4**, 1 (1972).
[9] M. Takahashi, N. Watanabe, Y. Khajuria, K. Nakayama, Y. Udagawa, and J. H. D. Eland, J. Electron Spectrosc. Relat. Phenom. **141**, 83 (2004).
[10] M. Takahashi, N. Watanabe, Y. Khajuria, Y. Udagawa, and J. H. D. Eland, Phys. Rev. Lett. **94**, 213202 (2005).
[11] A. Senftleben, T. Pflüger, X. Ren, O. Al-Hagan, B. Najjari, D. Madison, A. Dorn, and J. Ullrich, J. Phys. B: At., Mol. Opt. Phys. **43**, 081002 (2010).
[12] A. Senftleben, O. Al-Hagan, T. Pflüger, X. Ren, D. Madison, A. Dorn, and J. Ullrich, J. Chem. Phys. **133**, 044302 (2010).
[13] X. Ren, T. Pflüger, S. Xu, J. Colgan, M. S. Pindzola, A. Senftleben, J. Ullrich, and A. Dorn, Phys. Rev. Lett. **109**, 123202 (2012).
[14] E. Ali, X. Ren, A. Dorn, C. Ning, and D. Madison, J. Phys. B: At., Mol. Opt. Phys. **48**, 115201 (2015).
[15] J. Lower, J. Baxendell, and S. Bellm, in *Nanoscale Interactions and Their Applications: Essays in Honour of Ian McCarthy*, edited by F. Wang and M. J. Brunger (Transworld Research Network, Kerala, India, 2007), Chap. 9, pp. 95–106.
[16] S. Bellm, J. Lower, D. Mueller, and E. Weigold, J. Phys.: Conf. Ser. **212**, 012005 (2010).
[17] S. Bellm, J. Lower, E. Weigold, and D. W. Mueller, Phys. Rev. Lett. **104**, 023202 (2010).
[18] J. C. A. Lower, E. Ali, S. Bellm, E. Weigold, A. Harris, C. G. Ning, and D. Madison, Phys. Rev. A **88**, 062705 (2013).
[19] D. B. Jones, M. Yamazaki, N. Watanabe, and M. Takahashi, Phys. Rev. A **87**, 022714 (2013).
[20] E. Shigemasa, J. Adachi, M. Oura, and A. Yagishita, Phys. Rev. Lett. **74**, 359 (1995).
[21] T. Weber, A. O. Czasch, O. Jagutzki, A. K. Müller, V. Mergel, A. Kheifets, E. Rotenberg, G. Meigs, M. H. Prior, S. Daveau, A. Landers, C. L. Cocke, T. Osipov, R. Díez Muiño, H. Schmidt-Böcking, and R. Dörner, Nature **431**, 437 (2004).
[22] N. Watanabe, S. Yamada, and M. Takahashi, Phys. Rev. A **95**, 060702(R) (2017).
[23] N. Watanabe, S. Yamada, and M. Takahashi, Phys. Chem. Chem. Phys. **20**, 1063 (2018).
[24] P. W. Erdman and E. C. Zipf, Rev. Sci. Instrum. **53**, 225 (1982).
[25] M. Takahashi, N. Watanabe, Y. Wada, S. Tsuchizawa, T. Hirosue, H. Hayashi, and Y. Udagawa, J. Electron Spectrosc. Relat. Phenom. **112**, 107 (2000).
[26] R. Herzog, Z. Phys. **97**, 596 (1935).
[27] See http://www.roentdek.com/ for information about the DLD40 and DLD80 position sensitive detectors and the TDC8 PCI2 time-to-digital converter.
[28] J. N. H. Brunt, F. H. Read, and G. C. King, J. Phys. E: Sci. Instrum. **10**, 134 (1977).
[29] A. T. J. B. Eppink and D. H. Parker, Rev. Sci. Instrum. **68**, 3477 (1997).
[30] M. Lebech, J. C. Houver, and D. Dowek, Rev. Sci. Instrum. **73**, 1866 (2002).
[31] W. C. Wiley and I. H. McLaren, Rev. Sci. Instrum. **26**, 1150 (1955).
[32] See http://wwww.simion.com/ for information about SIMION 8.0.
[33] E. Wang, X. Shan, Y. Shi, Y. Tang, and X. Chen, Rev. Sci. Instrum. **84**, 123110 (2013).
[34] R. Singh, P. Bhatt, N. Yadav, and R. Shanker, Meas. Sci. Technol. **22**, 055901 (2011).
[35] A. Pandey, P. Kumar, S. B. Banerjee, K. P. Subramanian, and B. Bapat, Phys. Rev. A **93**, 042712 (2016).
[36] E. Shigemasa, K. Ueda, Y. Sato, T. Sasaki, and A. Yagishita, Phys. Rev. A **45**, 2915 (1992).
[37] R. Camilloni, E. Fainelli, G. Petrocelli, and G. Stefani, J. Phys. B: At. Mol. Phys. **20**, 1839 (1987).
[38] W. Butscher, R. J. Buenker, and S. D. Peyerimhoff, Chem. Phys. Lett. **52**, 449 (1977).
[39] T. N. Rescigno and A. E. Orel, J. Chem. Phys. **70**, 3390 (1979).
[40] R. Locht, W. Denzer, E. Rühl, and H. Baumgärtel, Chem. Phys. **160**, 477 (1992).
[41] C. Adamo and V. Barone, J. Chem. Phys. **110**, 6158 (1999).
[42] T. H. Dunning, Jr., J. Chem. Phys. **90**, 1007 (1989).
[43] D. E. Woon and T. H. Dunning, Jr., J. Chem. Phys. **103**, 4572 (1995).
[44] M. W. Schmidt, K. K. Baldridge, J. A. Boatz, S. T. Elbert, M. S. Gordon, J. H. Jensen, S. Koseki, N. Matsunaga, K. A. Nguyen, S. J. Su, T. L. Windus, M. Dupuis, and J. A. Montgomery, J. Comput. Chem. **14**, 1347 (1993).
[45] Y. Imamura, T. Otsuka, and H. Nakai, J. Comput. Chem. **28**, 2067 (2007).
[46] M. F. Ciappina, O. A. Fojón, and R. D. Rivarola, J. Phys. B: At., Mol. Opt. Phys. **47**, 042001 (2014), and references therein.

[47]N. Watanabe, X. J. Chen, and M. Takahashi, Phys. Rev. Lett. **108**, 173201 (2012).
[48]N. Watanabe, M. Yamazaki, and M. Takahashi, J. Electron Spectrosc. Relat. Phenom. **209**, 78 (2016).
[49]J. W. McConkey, C. P. Malone, P. V. Johnson, C. Winstead, V. McKoy, and I. Kanik, Phys. Rep. **466**, 1 (2008).
[50]P. Bhatt, R. Singh, N. Yadav, and R. Shanker, Phys. Rev. A **84**, 042701 (2011).
[51]J. N. Bull, J. W. L. Lee, and C. Vallance, Phys. Rev. A **91**, 022704 (2015).
[52]J. Lower, R. Panajotović, S. Bellm, and E. Weigold, Rev. Sci. Instrum. **78**, 111301 (2007), and references therein.